RSC Advances

PAPER

View Article Online
View Journal | View Issue

Cite this: *RSC Adv.*, 2023, **13**, 6287

Synthesis and comparative study of the structural and optical properties of binary ZnO-based composites for environmental applications†

B. Ben Salem, *[a] G. Essalah,[a] S. Ben Ameur,[a] B. Duponchel,[b] H. Guermazi,[a] S. Guermazi[a] and G. Leroy[b]

The development of photoactive systems to solve serious environmental problems is a key objective of researchers and remains a real challenge. Herein, n–p heterojunction ZnO-based composites were developed to achieve better photocatalytic performance in methylene blue (MB) degradation under natural solar irradiation. The hydrothermal technique was used to synthesize zinc oxide (ZnO)/metal oxide (MO) composites, with a molar ratio of 1 : 1 (MO = Mn_3O_4; Fe_3O_4; CuO; NiO). Various characterization techniques were used for the analysis of the structural, morphological and optical properties. X-ray diffraction (XRD), Scanning Electron Microscopy (SEM), Energy Dispersive X-ray Spectroscopy (EDX) Diffuse Reflectance Spectroscopy analysis (DRS), and Diffuse Reflectance Spectroscopy analysis (DRS) validated the presence of two phases for each sample, excluding any impurities. Indeed, the ZnO structure was not affected by the coupling with MO, confirming that MO was well dispersed on the surface of the ZnO crystalline lattice for each composite. Eventually, the photocatalytic performance evaluation test of the synthesized photocatalysts was carried out on aqueous MB solution. According to the results, the ZnO/Fe_3O_4 nano-catalyst showed the best photodegradation efficiency. This result suggests that the formation of Fe_3O_4/ZnO as a p/n heterojunction reduces the recombination of photo-generated electron/hole pairs and broadens the solar spectral response range, resulting in significant photocatalytic efficiency. Meanwhile, the possible mechanism for degradation of the MB was discussed.

Received 8th December 2022
Accepted 27th January 2023

DOI: 10.1039/d2ra07837f

rsc.li/rsc-advances

1. Introduction

During the various industrial processes of the textile industry, significant quantities of organic compounds are released into the wastewater, which increases environmental pollution.[1,2] Moreover, this phenomenon is considered to be one of the most important causes of water contamination, which can have harmful effects on humans and surrounding wildlife.[3] In particular, methylene blue (MB) is one of among the hazardous and non-biodegradable organic substances frequently used in the textile industries. Moreover, its planar structure makes it highly soluble in water.[4,5] Therefore, photocatalytic degradation of MB can be very beneficial to ensure environmental friendliness. In this regard, continuous efforts are made by researchers to develop efficient semiconductor photocatalysts that limit the use of sacrificial agents (H_2O_2) under natural solar irradiation. Indeed, the use of sacrificial agents for the degradation of organic pollutants is not cost-effective.[6,7]

Various n-type semiconductor photocatalysts like ZnO and TiO_2 have been used to develop photocatalysts for dye degradation.[8,9] Compared to TiO_2, many studies have focused on ZnO for the treatment of many toxic pollutants.[10–12] Due to its remarkable properties, such as low cost, high oxidation, non-toxic nature, high stability to photocorrosion and abundance in nature, zinc oxide is considered the most potential candidate for conversion of solar energy into a useful form of chemical or electrical energy.[13] However, unmodified zinc oxide is not considered a strong photocatalyst under visible light due to its relatively high band gap (~3.37 eV) and rapid charge carrier recombination rate.[14,15] Its practical use is strongly limited because it is active in ultraviolet light, which covers about 5% of the solar spectrum.

Therefore, solving this problem is essential to achieve efficient and fast performance. In this context, several studies have been initiated to improve the visible light absorption and electron–hole separation of ZnO by doping with a metal, a non-metal or by coupling with another metal oxide, a non-metal oxide.[16,17] One of the fundamental mechanisms of visible light

[a]*Laboratory of Materials for Energy and Environment, and Modelling, Faculty of Science, University of Sfax, Soukra Road km 4 PB 1171, 3038 Sfax, Tunisia. E-mail: basmabensalem1993@gmail.com*

[b]*Unity of Dynamic and Structure of Molecular Materials (UDSMM), Littoral Côte d'Opale (ULCO) University, Calais, France*

† Electronic supplementary information (ESI) available. See DOI: https://doi.org/10.1039/d2ra07837f

photocatalysis is the ability to initiate electron transfer, resulting in the generation of reactive oxygen species (ROS). These species are often responsible for the degradation of pollutants.

Among them, the p–n junction plays a key role in improving the performance of photodetectors, due to the effect of the integrated electric field generated at the interface, which allows better separation of the photoexcited electron–hole pairs.[18,19]

Heterojunction of ZnO with other metal oxides with different band edge positions is an excellent strategy to amplify carrier generation and separation under light illumination. All studies have shown that the heterojunction between metal oxides and ZnO improves the stability and reduces the charge transfer resistance in the synthesized particles. In particular, the coupling of ZnO (n-type) with another metal oxide (p-type) can lead to a change in the band gap and results in the separation of electron (e^-)–hole (h+) pairs under irradiation. Therefore, the electron–hole recombination rate is eliminated and thus higher photocatalytic activity.[20]

Among the various p-type semiconductor, manganite oxide (Mn_3O_4), iron oxide (Fe_3O_4) copper oxide (CuO) and nickel oxide (NiO) are recognized as remarkable co-catalysts to improve the photocatalytic performance of ZnO, due to its interesting electrical, optical and magnetic properties.[21–24] On the one hand, NiO is considered as one of the most important p-type semiconductors with gap energy equal to 3.5 eV, which has been widely used in photocatalytic applications. It can improve the efficiency of photocatalytic system for electron–hole pair generation and enhance the photo-decomposition kinetics by coupling with ZnO.[25] On the other hand, Mn_3O_4, Fe_3O_4 and CuO are important p-type semiconductors with band gaps equal to 2, 2.12, 1.4 respectively.[26–28] They have excellent properties including a strong carrier concentration, superior stability and light absorption in the visible region. For a ZnO/MO composite, ZnO regions of type n collect positive charges, whereas MO regions of type p collect negative charges. As a result, charge balance is achieved, leading to better separation of interfacial charge separation and longer charge carrier lifetimes. Therefore, ZnO/MO heterostructures have attracted increasing interest.[29–31]

Many physical and chemical synthesis methods are used to prepare heterostructured systems, including sol–gel, hydrothermal, co-precipitation and spray pyrolysis. A. E. Ramírez *et al.*[32] are synthesized mixed photocatalysts from transition metal oxides (TMOs), such as Cr_2O_3, MnO_2, FeO, CoO, NiO, Cu_2O, CuO, and ZnO by the sol–gel method. E. D. Sherly *et al.*[33] are successfully synthesized some coupled oxides, ZnO–MO (MO = CuO, NiO, ZrO_2 and CeO_2) using a microwave assisted one pot solution combustion synthesis, which favored the separation of photogenerated carriers. Unlike physical or chemical vaporization methods, hydrothermal synthesis is a simple, cost-effective, and environmentally friendly synthesis route, which is also suitable for mass preparation in industrial production, including synthesis by low-temperature hydrothermal reactions.[34,35] Therefore, the hydrothermal method was used to obtain high-quality ZnO-based binary composites.

This work consists in presenting a comparison of the functional properties of ZnO coupled to metal oxides (MO = Fe_3O_4, Mn_3O_4, CuO, NiO) for environmental applications. The ZnO heterostructures coupled to the MO were prepared by the hydrothermal procedure under the same conditions. The nature and structural parameters were determined by an X-ray diffraction analysis. UV-visible DRS measurements were performed to estimate the optical gap values and to explore the change in optical properties of ZnO as a result of the coupling process with different metal oxides. In addition, Fourier transform infrared (FT-IR) curves were recorded to evaluate the vibrational variation of the samples. The surface morphology and the elemental analysis of the different heterostructures of ZnO coupled to the MO were explored by scanning electron microscopy. Based on all these results, we provide some information on the photocatalytic activity under sunlight for the degradation of MB using these binary metal oxides.

2. Methodology

2.1. Materials

In order to prepare the different binary composites, zinc chloride ($ZnCl_2$), manganese(II) chloride tetrahydrate ($MnCl_2\ 4H_2O$), iron(II) sulfate heptahydrate ($FeSO_4 \cdot 7H_2O$), copper sulfate pentahydrate ($CuSO_4 \cdot 5H_2O$), nickel sulfate hexahydrate ($NiSO_4 \cdot 6H_2O$) and sodium hydroxide (NaOH), were used as starting materials and distilled water as solvent. Methylene blue (MB) dye was used as an organic contaminant.

All these products were of analytical grade (purity >99%). They were obtained from Sigma Aldrich, and no further purification was performed on them.

2.2. Synthesis details

The ZnO-based composites were synthesized by a facile one-step hydrothermal route. The successive steps involved in the fabrication of the ZnO/MO (MO = Mn_3O_4, Fe_3O_4, CuO and NiO) composites are described in Fig. 1.

First, 2 g of zinc chloride ($ZnCl_2$) and a very specific mass of second precursor ($MnCl_2 \cdot 4H_2O$, $FeSO_4 \cdot 7H_2O$, $CuSO_4 \cdot 5H_2O$, or $NiCl_2 \cdot 6H_2O$), with a molar ratio of 1 : 1, were dissolved in 20 ml of distilled water under magnetic stirring at room temperature. Then, 10 ml of NaOH was added drop-wise to the mixed solution every 10 min, then the pH was adjusted to 8 during the process. After 30 min of stirring, the solution was transferred to a Teflon-coated stainless steel autoclave of 50 ml capacity. The autoclave was sealed and heated at 110 °C for 24 hours in an oven and then naturally cooled to room temperature. After the hydrothermal reaction, colored precipitates were formed at the bottom of the autoclave. These precipitates were filtered and rinsed several times with ethanol and distilled water to remove unreacted compounds. Then, they were filtered and dried at 80 °C for 12 hours. Finally, the dried powders were ground. After drying, the obtained samples are in amorphous form. It is therefore necessary to carry out a thermal treatment to obtain crystalline structures and to eliminate all traces of organic chains and solvents. This treatment was performed in an oven, equipped with a programmable temperature controller ($T = 500$ °C/$t = 5$ h).

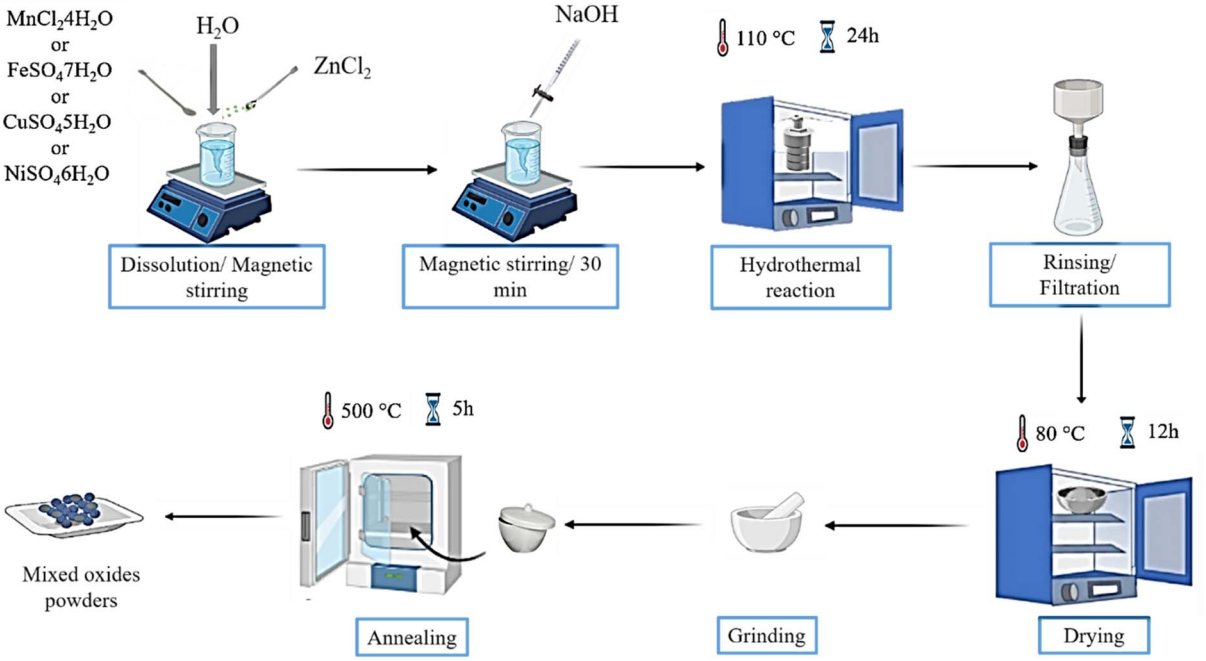

Fig. 1 Schematic diagram describing the preparation steps of the preparation of ZnO/MO composites.

The obtained powders were then used for further characterization.

2.3. Photocatalytic experiment

The photocatalytic activity of the binary composites (ZnO/Mn_3O_4, ZnO/Fe_3O_4 ZnOCuO and ZnO/NiO) was evaluated by degradation of an aqueous solution of the methylene blue MB dye (5 ppm) at room temperature under sunlight (time: 11:00 am to 2:00 pm). A total of 50 mg of each photocatalyst powders was loaded into 60 ml of simulating pollutant MB with a concentration of 5 mg l^{-1}. The suspension was magnetically stirred for 60 min in the dark to ensure complete equilibration of adsorption/desorption between the catalyst surface and the organic dye. After this, the suspension was placed under sunlight. Then, each aliquot (~2 ml) was taken every 30 min, filtered and centrifuged at 6000 rpm for 20 min to separate the catalytic precipitate from the dye solution. Finally, the concentration of MB was monitored by measuring the absorption intensity at 664 nm, using a UV-visible spectrophotometer.

2.4. Characterization

The structural investigations of the prepared samples were carried using a powder X-ray diffractograms (2θ = 5°–70°, Phillips powder diffractometer operating with copper Kα radiation source/λ = 1.54060 Å). The obtained XRD data were processed with X'Pert HighScore software, where the Miller indices (hkl) and their corresponding interplanar distance (d_{hkl}) were identified.

The presence of the metal-oxide groups was studied using a PerkinElmer Fourier Transform Infrared (FT-IR) Spectrometer in transmission mode, in the range 400–4000 cm^{-1}.

The morphological properties and the surface elemental composition (energy dispersive X-ray spectrum) of the synthesized samples were obtained using a scanning electron microscope (Model JEOL JSM7100F) coupled with EDX spectrometer using double-faced adhesive carbon pads (AGG3347N from Agar Scientific). In order to estimate the average grain size, the Image J software was then used.[36]

The optical properties were studied in the form of pellets using a UV-vis diffuse reflectance spectrophotometer (Model Perkin- ELMER 365, 300–800 nm). The reflectance spectra were recorded between 300 and 800 nm. The photoluminescence measurements were recorded using a Jobin Yvon HR 250 spectrometer at room temperature with an excitation of 266 nm.

The optical absorption spectra were measured by a Shimadzu UV-1800 UV-visible spectrophotometer.

3. Results and discussion

3.1 Characterization of the prepared materials

Knowing the key factors involved in photocatalytic activity will help explore the use of MO coupled ZnO in environmental applications. Therefore, it is necessary to determine the relevant physicochemical parameters including crystallite size, shape, composition, morphology and optical gap that could be advantageously related to the photocatalytic activity.

3.1.1 Powder X-ray diffraction study. The crystallinity, phase and purity of the ZnO samples combined with Mn_3O_4, Fe_3O_4, CuO and NiO were examined by powder XRD as shown in Fig. 2. Peaks at 2θ of: 31.6 (100), 34.3 (002), 36.2 (101), 47.4 (102), 56.5 (110), 62.7 (103), 67.8 (112), and 69.1° (203) are assigned to hexagonal wurtzite ZnO, space group $P6_3mc$ (ICDD card no. 01-080-0074). In addition to the primary phase of ZnO, reflections

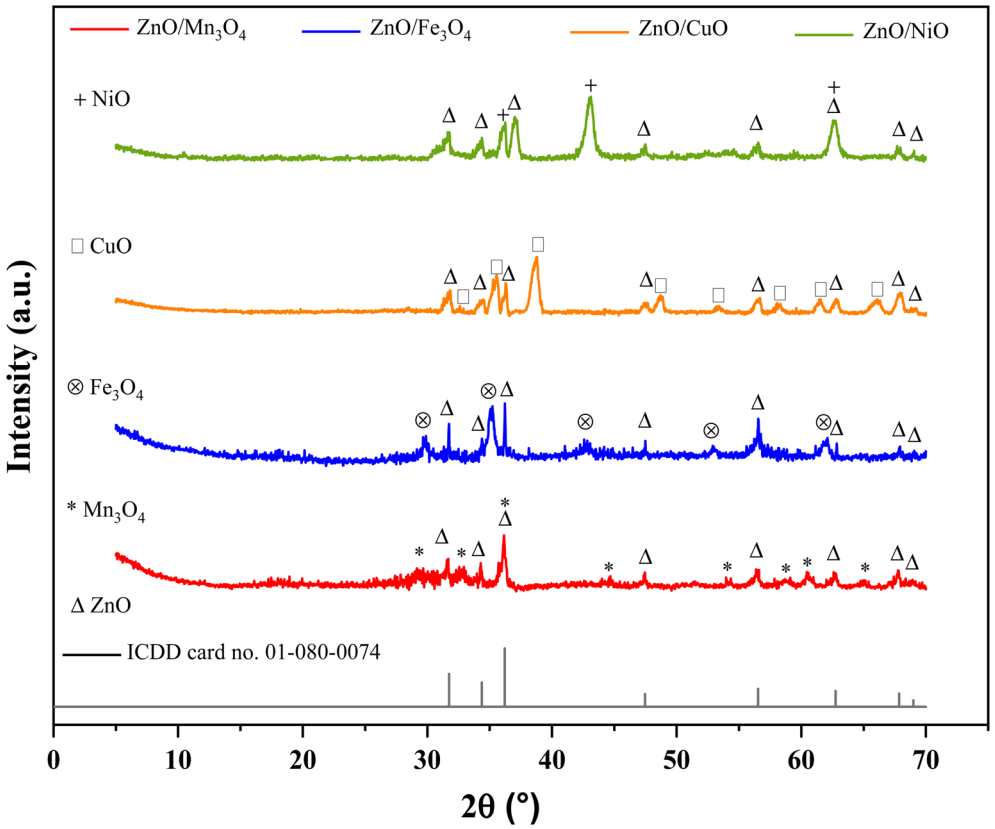

Fig. 2 X-ray diffraction patterns of ZnO/MO powders.

related to the secondary phase of the transition metal oxide are determined. Each composite is therefore a mixture of individual binary oxide phases coexisting in a single material. The $I4_1/amd$ space group diffraction peaks of the manganese oxide Mn_3O_4 phase corresponding to the tetragonal structure (ICDD card no. 00-001-1127) are observed at 2θ of: 29.1 (112), 32.8 (103), 36.2 (211), 44.3 (220), 51.1 (105), 54.1 (312), 58.7 (321), 60.5 (224), and 64.9° (314). The $Fd\bar{3}m$ space group peaks of the manganite Fe_3O_4 phase corresponding to the cubic structure (ICDD card no. 01-089-0688) are appeared at 2θ of: 29.8 (220), 35.1 (311), 42.7 (400), 52.8 (422), and 62.1° (440). The peaks in the $C2/c$ space group of the CuO copper oxide phase corresponding to the monoclinic structure (ICDD card no. 01-080-1268) are exhibited at 2θ of: 32.5 (110), 35.6 (−111), 38.7 (111), 48.8 (−202), 53.3 (020), 58.1 (202), 61.5 (−113), and 66.2 (−311). On the other hand, the peaks at 2θ of: 37.2 (111), 43.2 (200), and 62.7° (220) are assigned to the cubic nickel oxide phase NiO, space group $Fm\bar{3}m$ (ICDD card no. 01-073-1523). Moreover, there is no additional phase or impurity detected, which implies that the obtained materials have high degree of crystallinity.[37–40]

The lattice constants (a, b and c) were calculated using the following formulas:

$$2d\sin\theta = n\lambda \quad (1)$$

For ZnO (hexagonal structure):

$$\frac{1}{d^2} = \left(h^2 + k^2 + l^2\left(\frac{a}{c}\right)^2\right) + \frac{1}{a^2} \quad (2)$$

For Mn_3O_4 (tetragonal structure):

$$\frac{1}{d^2} = \frac{4}{3}\left(\frac{h^2 + hk + k^2}{a^2}\right) + \frac{l^2}{c^2} \quad (3)$$

For Fe_3O_4 and NiO (cubic structure):

$$\frac{1}{d^2} = \left(\frac{h^2 + k^2 + l^2}{a^2}\right) \quad (4)$$

For CuO (monoclinic structure):

$$\frac{1}{d^2} = \frac{1}{\sin^2\beta}\left(\frac{h^2}{a^2} + \frac{k^2\sin^2\beta}{b^2} + \frac{l^2}{c^2} - \frac{2hl\cos\beta}{ac}\right) \quad (5)$$

where d is the inter-planar distance, h, k and l are the Miller indices. θ is Bragg's angle of diffraction, and λ is the incident radiation wavelength.

Table 1 groups the structural parameters obtained for the different binary composites. The values of the structural parameters of the ZnO phase are according to the data of the ICDD card no. 01-080-0074. In all cases, the static structure factor of the wurtzite phase ($c/a \sim 1.602$) remains constant. This indicates that virtually no change was observed in the lattice

Table 1 Lattice parameters and average crystallite size of the phases obtained from XRD diagrams

	Wurtzite phase (ZnO)				Metal oxide phase (MO)			
Catalyst	a (Å)	c (Å)	a/c	D (nm)	a (Å)	b (Å)	c (Å)	D (nm)
ZnO/Mn_3O_4	3.2519	5.2108	1.6023	18.93	57 500	57 500	92 401	13.14
ZnO/Fe_3O_4	3.2531	52 123	1.6022	21.53	8.4903	8.4903	8.4903	17.20
ZnO/CuO	3.2524	5.2116	1.6023	16.83	4.6792	3.4213	5.1301	13.16
ZnO/NiO	3.2541	5.2138	1.6022	10.63	4.1683	4.1683	4.1683	13.03

constants of the ZnO phase, implying that the metal oxide did not diffuse into the ZnO structure, as has been reported in the literature. In fact, the diffusion led to the substitution of Zn ions by transition metal ions and caused changes in the lattice constants of the ZnO structure, which was not observed.[41] Therefore, the Mn_3O_4, Fe_3O_4, CuO and NiO particles are well dispersed on the ZnO surface for each composite.

The Debye–Scherer equation was used to determine the average crystallite size (D) and dislocation density (δ).[42]

$$D = \frac{k\lambda}{\beta \cos \theta} \quad (6)$$

where K is the Scherer constant, is λ the X-ray wavelength for the copper source equal to 1.5406 Å, θ is the Bragg angle and β is the full-width at half-maximum (in radians).

The average crystallite size for the ZnO phase coupled to manganese oxide, iron oxide, copper oxide and nickel oxide, was 18.93, 21.53, 16.83 and 10.63 nm, respectively. A diversification of ZnO intensity in different samples can be observed, however, which can affect the FWHM, resulting in a different crystallite size. These values are lower than those reported in literature for powders prepared by other methods, proving the importance of hydrothermal technique.

3.1.2 Fourier transform infrared analysis. The presence of functional groups on the surface of catalysts was confirmed by infrared spectroscopy. Fig. 3a shows the FT-IR spectra for the prepared composites in the range (400–4000 cm^{-1}). However, to clarify the region of interest, the FT-IR spectra are enlarged in a precise range of 400–1400 cm^{-1} (Fig. 3b). Wide band at 3500–3000 cm^{-1} detected due to the stretching vibration of the hydroxyl group (O–H). The peak around 1635 cm^{-1} represents the bending modes of the OH group.[43] This is probably a result of the atmospheric humidity affecting the samples when exposed for measurement, especially for ZnO/Fe_3O_4. This result plays an important role in the photodegradation mechanism.[44] Indeed, the adsorbed OH ions can trap charge carriers to produce reactive hydroxyl radicals ($OH^{\bullet}$), which function as active sites to remove organic dye molecules. Moreover, the broad band to 1063–1100 cm^{-1} indicates the existence of SO_4^{-2} in the IR spectrum of ZnO/Fe_3O_4, ZnO/CuO and ZnO/NiO composites.[45] Indeed, the precursors of copper and iron are the sulfate type ($CuSO_4 \cdot 5H_2O$/$FeSO_4 \cdot 7H_2O$). Generally, metal oxides give absorption bands below 1000 cm^{-1} arising from the inter-atomic vibrations.[46] Accordingly, the vibrational bands of the Zn–O bond are around 494, 512, 530 and 532 cm^{-1}.[47,48] The FT-IR spectrum corresponding to ZnO/Mn_3O_4 shows the presence of the vibrational band around 617 cm^{-1} attributed to the stretching mode of Mn–O.[49] Furthermore, IR bands for Cu–O stretching modes are observed at 429, 476, 583, 612 and 653 cm^{-1}.[45] For the IR spectrum of ZnO/Fe_3O_4, detected band in the infrared spectrum at 400 cm^{-1} can be attributed to the stretching vibration of Fe–O bonds.[50] On the other hand, NiO shows IR absorption peaks due to Ni–O vibration at 400 and 618 cm^{-1}.[51] No other active mode corresponding to other species such as $Zn(OH)_2$ was detected, in agreement with the XRD analysis which confirms the purity of the prepared samples. Thus, the FTIR spectrum analysis confirmed the presence of two distinct crystal phases in each ZnO/MO composite, which agrees well with the XRD results.

3.1.3 Surface morphology and elemental examinations. The surface morphology of the as-prepared coupled metal oxides, ZnO/MO (MO = Fe_3O_4, Mn_3O_4, CuO, NiO) was examined by scanning electron microscopy SEM analysis. Fig. 4a–d shows the SEM micrographs of ZnO/Mn_3O_4, ZnO/Fe_3O_4, ZnO/CuO and ZnO/NiO composites, respectively. The two samples ZnO/Mn_3O_4 and ZnO/CuO tend to have quasi-spherical shapes with an inhomogeneous distribution with micrometer dimension size that varies between. While, the SEM images of ZnO/Fe_3O_4 and ZnO/NiO reveals clear nanoparticles of spherical shape. Histograms of the particle distribution constructed by Image J software are used to calculate the average particle size (Fig. 4 (inset)). Regarding the particle distribution of Mn_3O_4, CuO and NiO coupled ZnO particles, the particles do not possess a uniform size distribution as shown in the histograms. However, this agglomeration is negligible for Fe_3O_4 coupled ZnO. According to Table 2, these statistics indicate that the particle size is nanometric for iron oxide and nickel oxide and micrometric for manganese oxide and copper oxide. Therefore, ZnO/Fe_3O_4 and ZnO/NiO can have high specific surface area, which can enhance the adsorption of dye molecules to active adsorption sites in photocatalytic assays, as will be confirmed later.[52] Indeed, nanoscale materials have a large active surface area, which promotes the adsorption of organic pollutants and thus improves photocatalytic performance.[53,54]

Moreover, the prepared powders were examined by EDX to identify the qualitative chemical composition. Fig. 4 shows the EDX diagrams of Fig. 4e ZnO/Mn_3O_4, Fig. 4f ZnO/Fe_3O_4, Fig. 4g ZnO/CuO and Fig. 4h ZnO/NiO. These EDX spectra reveal the presence of "Zn", "Fe", "Mn", "Cu", "Ni" and "O" signals. Moreover, the presence of carbon "C" in the spectra obtained

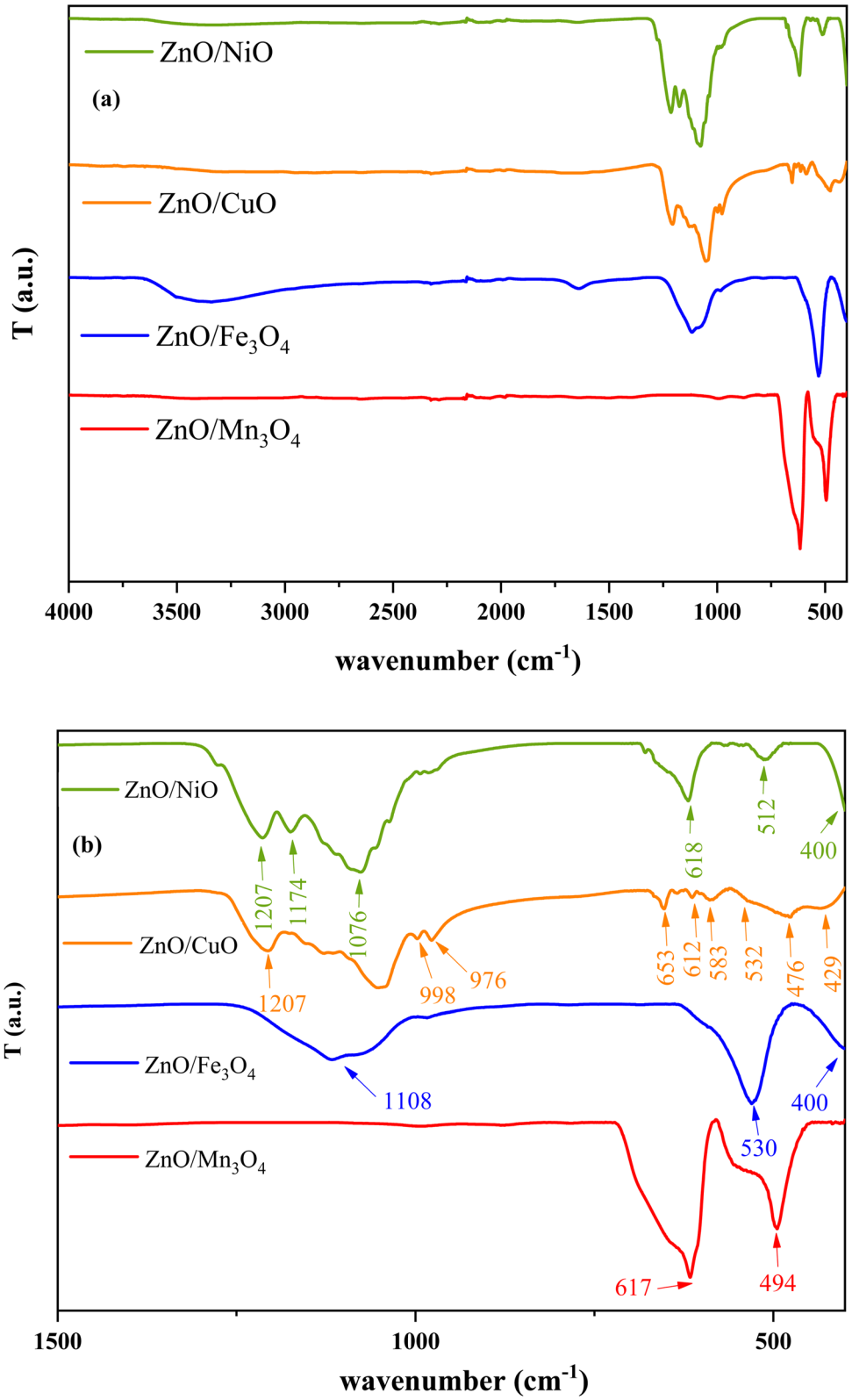

Fig. 3 FTIR spectra of ZnO/MO composites (a) in the range 400–4000 cm^{-1}, and (b) magnified spectra from 400 to 1500 cm^{-1}.

for all the samples Fig. 4) is due to the conductive carbon substrate used as a support during the analysis (see Fig. 4i). No elemental impurities were found within the EDX detection limit. This indicates that the high purity and good crystallization of the fabricated composites are in agreement with the XRD and FT-IR results, confirming the successful formation of the various binary composites.

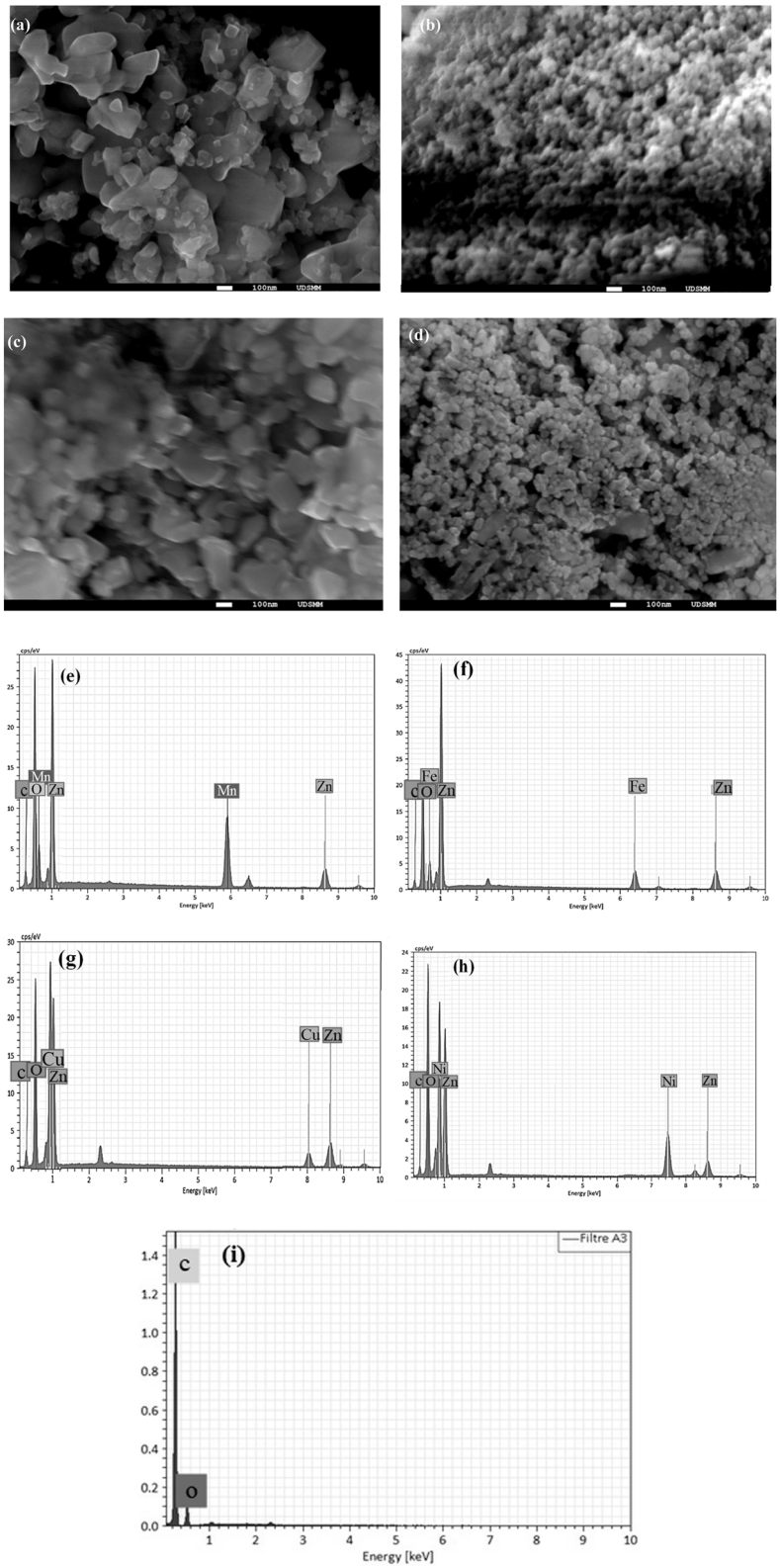

Fig. 4 SEM images and Size distribution (insert) of (a) ZnO/Mn_3O_4, (b) ZnO/Fe_3O_4, (c) ZnO/CuO and (d) ZnO/NiO and energy dispersive spectra/EDX of (e) ZnO/Mn_3O_4, (f) ZnO/Fe_3O_4, (g) ZnO/CuO, (h) ZnO/NiO and (i) Carbon spectra EDX.

3.1.4 Optical properties. The optical properties of a photocatalyst have an importance of its photocatalytic efficiency. For the higher photocatalytic performance of zinc oxide, the optical band gap should be shifted to the visible region for better photon harvesting sunlight.[55] DRS-UV-vis spectroscopy is used to identify the optical properties and band gap of all four photocatalysts.

Table 2 The average particle size of ZnO/MO composites

Composite	The average particle size (nm)
ZnO/Mn_3O_4	110
ZnO/Fe_3O_4	41
ZnO/CuO	170
ZnO/NiO	65

The Kubelka–Munk function $F(R)$ (eqn (7)), are presented in Fig. 5 as a function of wavelength.[56]

$$F(R) = \frac{(1-R)^2}{2R} \quad (7)$$

We notice the presence of two strong absorption edges for each composite: the first one marked by an inflection point around 570, 600, 750 and 350 nm related to the Mn_3O_4, Fe_3O_4, CuO and NiO phase respectively, and the second one at ~400 nm is related to the ZnO phase. The appearance of two kinds of characteristic absorption bands also confirms that each sample is a composite material composed of ZnO phase and other MO phase.

Band gap energy. To determine the gap energy (E_g) of the prepared nanoparticles, we used the Tauc's low (eqn (8)):[57]

$$(\alpha h\nu) = \beta(h\nu - E_g) \quad (8)$$

in which α is the absorption coefficient, calculated from the Kubelka–Munk function $F(R)$ through the following equation: $\alpha = \frac{F(R)}{t}$, $t = 1$ mm represents the thickness of the pellet, β is a constant independent of energy or band tailing parameter, h is the Planck's constant, ν is the incident light frequency, and p is the power factor. p-Value is governed by the optic transition type, it can take the following values: 1/2, 3/2, 2 or 3 for direct allowed, direct forbidden, indirect allowed or indirect forbidden transition, respectively. In our case, p is equal 1/2, since ZnO, Mn_3O_4, Fe_3O_4, CuO and NiO have a direct band gap, according to the literature.[26,58–60]

The optical band gap energy was calculated from extrapolating the linear region of the plot of $(\alpha h\nu)^2$ (x-axis) *vs.* $h\nu$ (y-axis) that was determined by the x-intercept (Fig. 6). The energy gap value E_g of the ZnO/Mn_3O_4, ZnO/Fe_3O_4, ZnO/CuO and ZnO/NiO

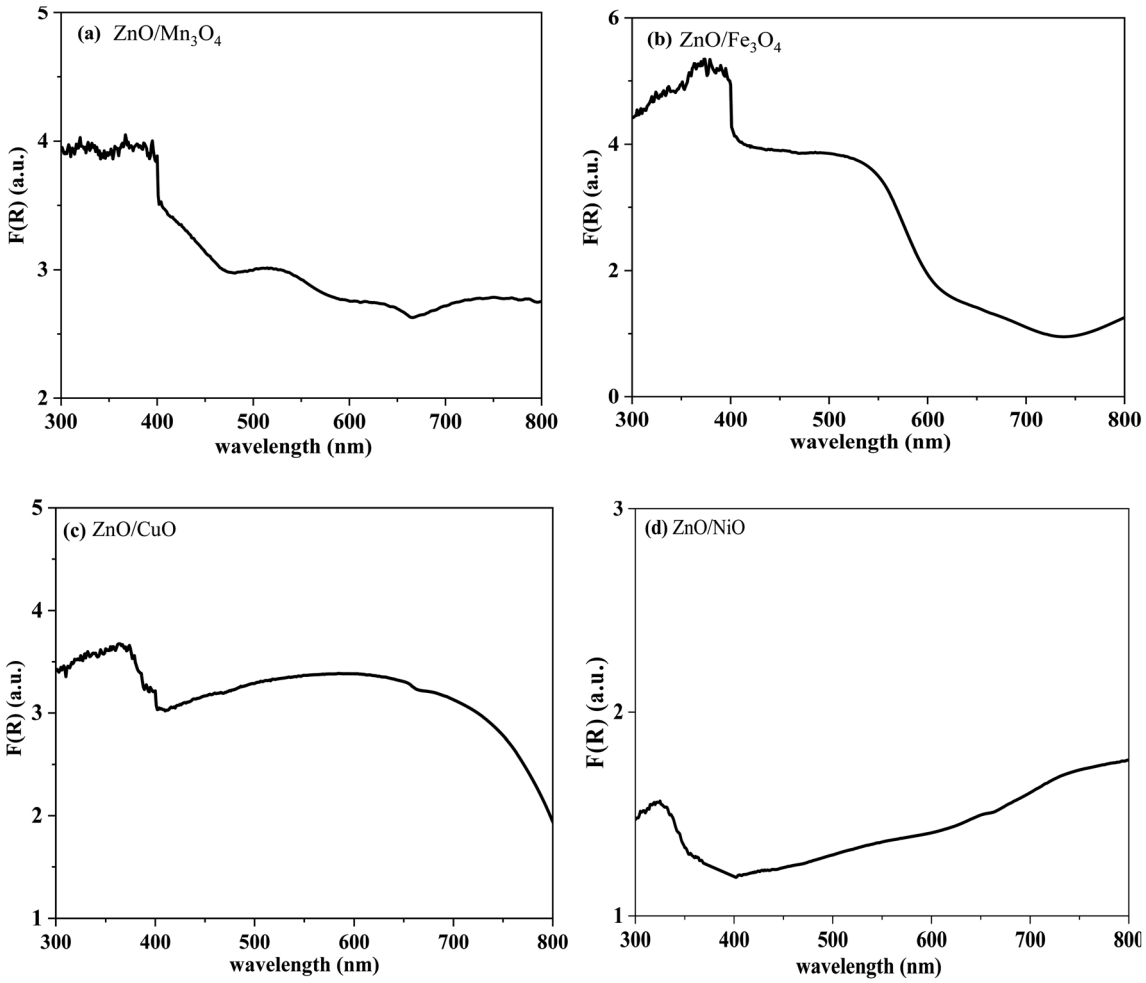

Fig. 5 Transformed Kubelka–Munk functions $F(R)$ *vs.* wavelength λ of (a) ZnO/Mn_3O_4, (b) ZnO/Fe_3O_4, (c) ZnO/CuO, (d) ZnO/NiO.

was found to be (2.99/2.17), (2.97/2.04), (3.02/1.47) and (3.03/3.31) eV, respectively (Table 3), which significantly lower than those reported in the literature.[26,60–62] The combination of ZnO with these metal oxides improved charge separation and increased light absorption. In addition, the creation of an n-p heterojunction between semiconductors with compatible band potentials improves the catalytic efficiency. In fact, the intimate interfaces can act as a transport channel, promoting the separation of electron–hole pairs. These interactions exert an influence on the charge carrier recombination times by forming new Fermi levels located between the valence band (VB) and the conduction band (CB), and thus electron transfer occurs in two steps: the first going from the VB to the local level in the energy band gap, and the second representing the additional jump to the CB.[63] Thus, it is possible to define a composite to meet the specific characteristics of use in photovoltaics and photocatalysis. The different ZnO/MO exhibited a lower band gap compared to pure ZnO (3.37 eV). It is possible that the uniform distribution and high ratio of Fe_3O_4 in the ZnO/Fe_3O_4 nanocomposite with small spherical shape are the causes of the reduction of the band gap energy of ZnO in the nanocomposite. Therefore, the coupling of ZnO and Fe_3O_4 with a ratio of 1 : 1 in a nanocomposite reduced the band gap energy and improved the photocatalytic activity of the composite under sunlight irradiation. In addition, ZnO/Fe_3O_4 was expected to have the fastest decomposition rate for organic compounds. Indeed, for nanomaterials with a lower band gap, electrons can more easily pass from the VB to the CB.

Table 3 Energy values Tables of ZnO/MO composites

Catalyst	Band gap energy (eV)	
	Wurtzite phase (ZnO)	Metal oxide phase (MO)
ZnO/Mn_3O_4	2.99	2.17
ZnO/Fe_3O_4	2.97	2.04
ZnO/CuO	3.02	1.47
ZnO/NiO	3.03	3.31

The presence of two optical gaps indicates the formation of n–p heterojunctions and subsequently the confirmation of the binary composite nature shown by XRD and FT-IR.

3.1.5 Photoluminescence study. The PL spectrum can reveal important information about surface defects, oxygen vacancies and surface states, which can significantly affect the photocatalytic process.[64] Fig. 7 shows the PL spectra of ZnO

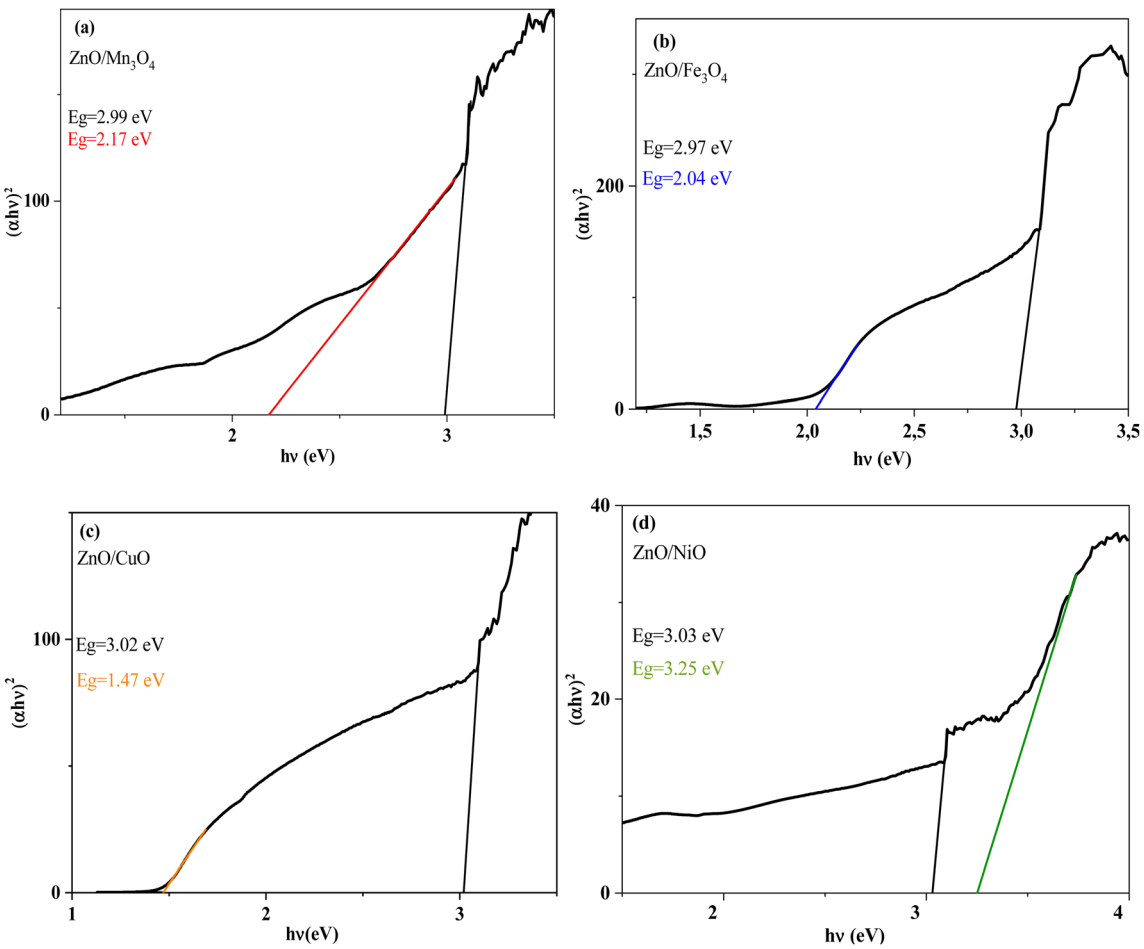

Fig. 6 The Tauc's plot $(\alpha h\nu)^2$ *vs.* photon energy ($h\nu$) for (a) ZnO/Mn_3O_4, (b) ZnO/Fe_3O_4, (c) ZnO/CuO, (d) ZnO/NiO.

coupled to OM at the excitation wavelength of 266 nm. Compared to ZnO/NiO, the PL intensity of ZnO/Mn_3O_4, ZnO/Fe_3O_4 and ZnO/CuO is remarkably low. This is due to the heterostructure (1 : 1) between ZnO and (Mn_3O_4, Fe_3O_4, CuO) which exhibit a response to visible excitation. The low excitation PL spectra show that defects are present in ZnO coupled to manganese oxide, iron oxide, and copper oxide. Unfortunately, they give information that does not allow for judging the quality of the composites. Fig. 8a shows the PL spectrum of ZnO/NiO nanocomposite and the Gaussian emission peak deconvolution. The high PL intensity in the UV region of the spectrum may be due to the rapid recombination of photo-induced electron–hole pairs in this region, while the broad PL peak located in the visible domain indicates an efficient separation of electrons and holes. Therefore, long-lived carriers are gotten in this region. The Gaussian adjustment of PL emission peaks of ZnO/NiO suggests the presence of several individual emissions. The emission peaks in the UV region at 326, 338, 352, and 382 nm are assigned to the emission from the wide band gap metal oxide (NBE). In addition, in the visible region, we observe a violet emission at 410 nm, blue emission at 453 nm, and green emission at 500 nm.

Fig. 8b illustrates the schematic band diagram for the PL electronic transitions present in ZnO/NiO nanocomposite. Since the E_g values (2.99 and 3.23 eV) are lower than the excitation (266 nm, 4.66 eV), an electron exhibited an electronic transition from the valence band (VB) to a high energy level, leaving a hole in this band. Then, this electron reached the conduction band (CB) by internal conversion (IC).[65] The violet emission at 410 nm (3.02 eV) is due to the transition of the electrons trapped at the metal interstitials (M_i) level to the VB. Besides, in a recent study, T. Tangcharoen *et al.*[66] showed that the blue luminescence peak appearing at 453 nm (~2.73 eV) identifies oxygen antisites (O_M) as acceptor defects in the ZnO/NiO nanocomposite. As they showed that emission at around 500 nm (~2.48 eV) occurred as a result of recombination

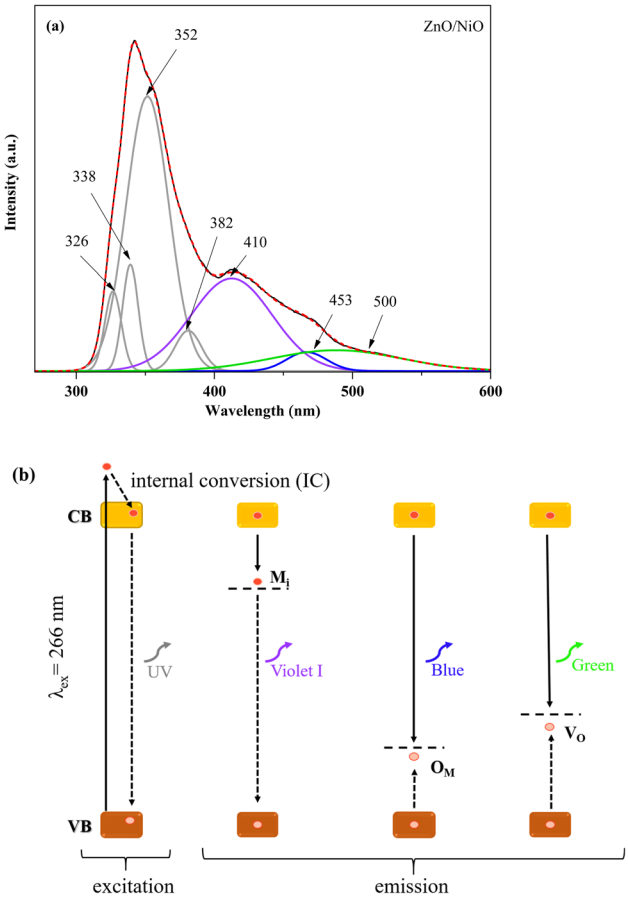

Fig. 8 (a) PL emission spectrum for 266 nm excitation wavelength, and (b) schematic band diagram representation of the measured PL emissions in ZnO/NiO composite.

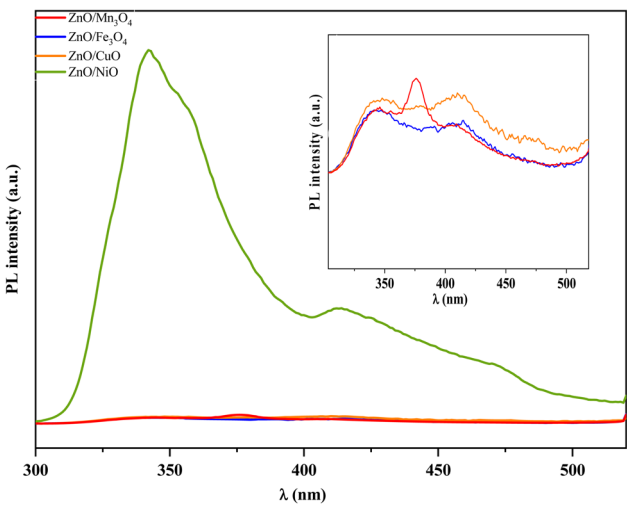

Fig. 7 PL emission spectrum of ZnO/Mn_3O_4, ZnO/Fe_3O_4, ZnO/CuO, ZnO/NiO at room temperature.

between the photogenerated hole, trapped in the deep oxygen vacancy and the photogenerated electron trapped in a shallow level, located below the CB.[67,68] The presence of oxygen vacancies reduces the effective electron mass, hence the increase in electron mobility.[69,70] Therefore, the separation of photo-induced electrons and holes will be enhanced in the nanocomposite, which can lead to enhanced photocatalytic activity. Similarly, Zhu *et al.* reported that the excellent photocatalytic properties are affected by the contribution of oxygen vacancies in ZnO.[71] In fact, the electrons confined by the V_O oxygen vacancies can react with the O_2 molecules and then produce the radicals responsible for perpetuating the degradation process.[72]

3.2 Photocatalytic activity study

For this work, the main task is the preparation of binary composites based on metal oxides with unique properties and photoactive under sunlight.

3.2.1 Effect of irradiation time. From the results obtained by UV-vis DRS spectroscopy, it is evident that the prepared composites (heterostructures) were active in the visible region. In order to evaluate the photocatalytic performance of ZnO/Mn_3O_4, ZnO/Fe_3O_4, ZnO/CuO and ZnO/NiO various tests are performed and the MB is taken as the standard pollutant for the

photocatalytic degradation under sunlight. The change in the intensity of the absorption peak recorded at $\lambda_{max} = 663$ nm was monitored to deduce the final performance.

The photodegradation rate η (%) of MB dye is calculated by the following relation:

$$\eta\ (\%) = \frac{A_0 - A}{A_0} \times 100 \quad (9)$$

In which A_0 is the absorbance of MB at t_0 when the adsorption–desorption equilibrium was completed, whereas A is the absorbance of MB at time t during the photocatalytic treatment.

The results obtained for the catalytic photodegradation of the MB dye tested by the four catalysts show a continuous increase in the percentage removal of the dye with increasing illumination time.

From the photocatalytic dye removal curves of MB dye (Fig. 9), the values of the photodegradation rate value using the photocatalysts ZnO/Mn_3O_4, ZnO/Fe_3O_4, ZnO/CuO and ZnO/NiO after 180 min under sunlight is 67, 76, 46 and 64%, respectively.

As a result, the ZnO/Fe_3O_4 nano-powder exhibits the best photocatalytic performance, which reached a maximum degradation after 180 min. This high photocatalytic performance of ZnO/Fe_3O_4 nano-powder is attributed to the collective effect of several factors. The XRD results clearly show that the ZnO/Fe_3O_4 nano-catalyst is well crystalline. Indeed, amorphous or semi-crystalline materials have a very low degradation rate compared to crystalline materials.[73,74] Moreover, the shape and particle size of the synthesized material play a key role to obtain a product with high photocatalytic performance because the shape affects the surface properties of the materials.[75–77] For ZnO/Fe_3O_4, SEM confirms the presence of spherical nanoparticles with a homogeneous distribution. In fact, several reports showed that spherical shaped particles have a higher degradation rate compared to other shapes of materials. So during solar irradiation, some of the nanoparticles could easily participate in the photocatalytic reaction, resulting a high performance. Fe_3O_4 has a band gap equal to 2.12 eV and its combination with ZnO limited their band gap to 2.97 eV. This allows it to absorb visible light wavelengths, which improves the photodegradation process under sunlight. We concluded that the synthesized ZnO/Fe_3O_4 nano-catalyst has a well crystalline structure, a homogeneous spherical shape and that the optical properties favor its use in the visible region and thus under solar irradiation. These different parameters have essentially contributed to reach a better degradation rate. On the other hand, the low photocatalytic activity of the ZnO/CuO composite can be attributed to the high band gap value of ZnO in this composite (3.02 eV) which cannot be activated well by visible light irradiation. In addition, their morphology has large quasi-spherical grains (>100 nm), which may also decrease the photocatalytic activity.

3.2.2 Kinetic. It is evident from Fig. 9 that the degradation of the tested MB organic dye increases with increasing irradiation time. In order to obtain a better comparison of the photocatalytic efficiencies of the prepared catalysts, a kinetic model analysis was performed.

The Langmuir–Hinshelwood (L–H) kinetic model can be applied according to the following formula:

$$\ln\frac{A}{A_0} = -kt \quad (10)$$

in which k indicates the photodegradation rate constant.

The fits of the catalytic photodegradation of MB dye using the different composites with the first-order model were evaluated by linear regression of $\ln(A_0/A)$ *versus* time t, as shown in Fig. 10. The slopes of the straight lines represent the catalytic photoreaction rate constants k_0. The obtained values of photodegradation rate constants and correlation coefficients (R_2) for all catalysts are listed in Table 4. The first-order kinetic model fits indicated that the ZnO/Fe_3O_4 catalyst has a high value of the kinetic rate constant ($k = 0.0078$ min^{-1}) with a good fit (R_2 =

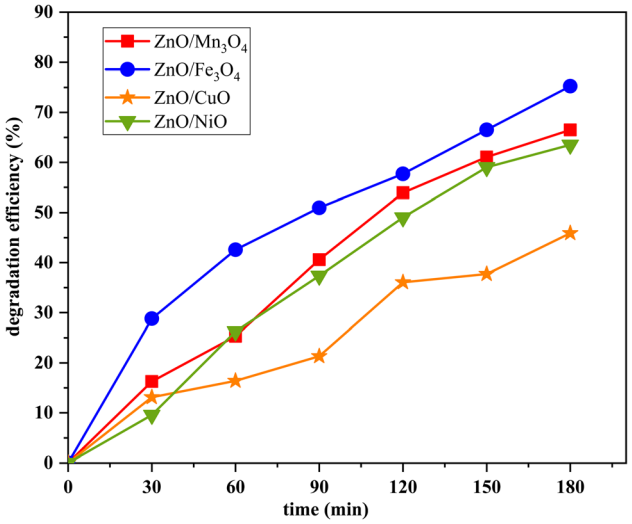

Fig. 9 The MB degradation rates as a function of sun-light illumination time.

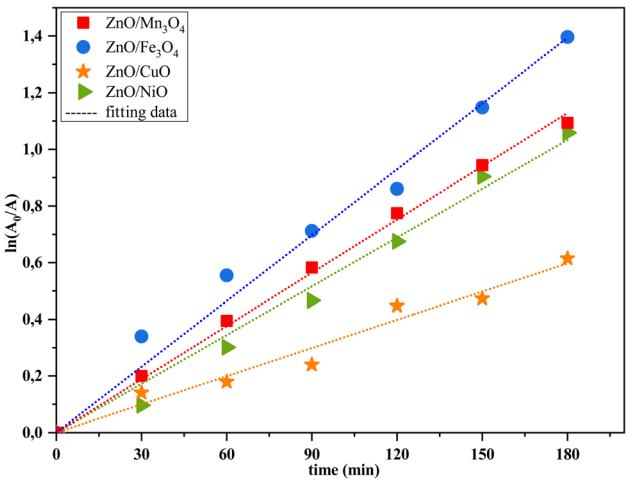

Fig. 10 The Langmuir–Hinshelwood model for the degradation kinetic of MB by ZnO/MO catalysts under sun-light irradiation.

Table 4 The kinetic parameters of the studied models for MB photodegradation using different catalysts

Catalysts	K (min^{-1})	R^2
ZnO/Mn_3O_4	0.0063	0.99
ZnO/Fe_3O_4	0.0078	0.98
ZnO/CuO	0.0033	0.97
ZnO/NiO	0.0057	0.99

0.98) compared to the other catalysts. This clearly shows that this catalyst has much better photocatalytic properties.

3.2.3 Comparison with previously reported works. A comparison of the photocatalytic activity of ZnO/MO (MO = Mn_3O_4; Fe_3O_4; CuO; NiO) for MB degradation with previously reported metal oxide photoactive materials is presented in Table 5. It is evident that our binary ZnO/MO photocatalysts studied in this work showed significantly significant photocatalytic performance compared to other catalytic systems.[78–86]

3.2.4 Proposed mechanism for the photocatalytic degradation. The mechanism of photocatalysis is based on the generation of electrons (e^-) and holes (h^+) under light excitation. For pure ZnO, electrons can be transferred to the conduction band which leads to the creation of holes in the valence band when ZnO is illuminated by UV light.[87] The photogenerated e^- and h^+ recombine to reach a lower energy level. Furthermore, the production and recombination of majority charge carriers are two processes that influence photocatalytic performance. Recombination of e^-/h^+ reduces carrier mobility and blocks the participation of the majority of charge carriers in reactions. Prior to recombination, electrons and holes are able to react with toxic molecules and break them down into non-toxic compounds as they migrate to the semiconductor (catalyst) surface.

The coupling of ZnO (n-type) with another metal oxide (p-type) results in the transport of electron–hole pairs between the two semiconductors, depending on the relative positions of the energy bands of ZnO and MO. In addition, the creation of the n–p junction interface {ZnO (n-type)/MO (p-type)} exerts a significant influence on the generation of carriers and the recombination process of electron–hole pairs.[88,89]

A schematic diagram of the photodegradation mechanism of ZnO/MO composites is shown in Fig. 11, describing the different electron transfers between ZnO and MO. When MO is associated with ZnO, a n–p heterojunction is created. Electrons can move from the n-type semiconductor (ZnO) to the p-type semiconductor (MO) by diffusion, while holes migrate in the opposite direction until equilibrium is reached in the composite. Simultaneously, the n–p semiconductor interface is the site of internal electric field generation. Under the effect of sunlight, the electrons in the valence bands (VB) of MO and ZnO are excited to those in the respective conduction bands (CB). In thermodynamic terms, there is a transfer of photogenerated electrons from the CB of MO to the CB of ZnO, while photogenerated holes are transferred in the opposite direction. As a result, more photogenerated electrons accumulate on the CB of ZnO. In the presence of oxygen, the electron is trapped, forming superoxide radicals that then react with water pollutants.

The photocatalytic mechanism occurs in three steps:[90,91]

➢ Oxidation

The reaction produced between h^+ and H_2O molecule or hydroxyl groups (OH^-) on the surface of the photocatalyst generated the hydroxyl radicals ($OH^\bullet$) and (H^+), according to the following reactions:

$$ZnO/MO + h\nu \rightarrow ZnO\ (e^- + h^+)/MO\ (e^- + h^+)$$

$$\text{n-type ZnO/p-type MO} + h\nu \rightarrow (e^-)_{ZnO} + (h^+)_{MO}$$

$$(h^+)_{MO} + OH^- \rightarrow OH^\bullet$$

$$(h^+)_{MO} + H_2O \rightarrow OH^\bullet + H^+$$

➢ Reduction

The dioxide (O_2) adsorbed on the surface of the photocatalyst is reduced by electrons (e^-) to produce superoxide species ($O_2^{\bullet -}$). The ($O_2^{\bullet -}$) undergoes successive reactions (I)–(IV) to give hydroxyl radicals ($OH^\bullet$), as shown by the following equations:

Table 5 Comparison of the degradation rates obtained in this work with other previous works

Catalyst	Pollutant	Light source	Degradation (%)	Time (min)	Reference
NiO	MB	Sunlight	17.7	60	78
ZnO	MB	Sunlight	68.6	135	79
ZnO NWs	MB	Sunlight	100	4320	80
ZnO/CuO (50 : 50)	MO	Visible light	27.7	120	81
Fe_3O_4/ZnO	RhB	Visible light	16	105	82
$ZnO/Eu_2O_3/NiO$ (1 : 1 : 1)	MB	UV light	80	150	83
Mn_3O_4	MB	HG lamp	21	240	84
ZnO/SnO_2	NOx	Solar lamp	20	60	85
ZnO/V_2O_4	MB	Xe arc lamp	90	400	86
ZnO/Mn_3O_4	MB	Sunlight	67	180	This work
ZnO/Fe_3O_4	MB	Sunlight	76	180	This work
ZnO/CuO	MB	Sunlight	46	180	This work
ZnO/NiO	MB	Sunlight	72.3	180	This work

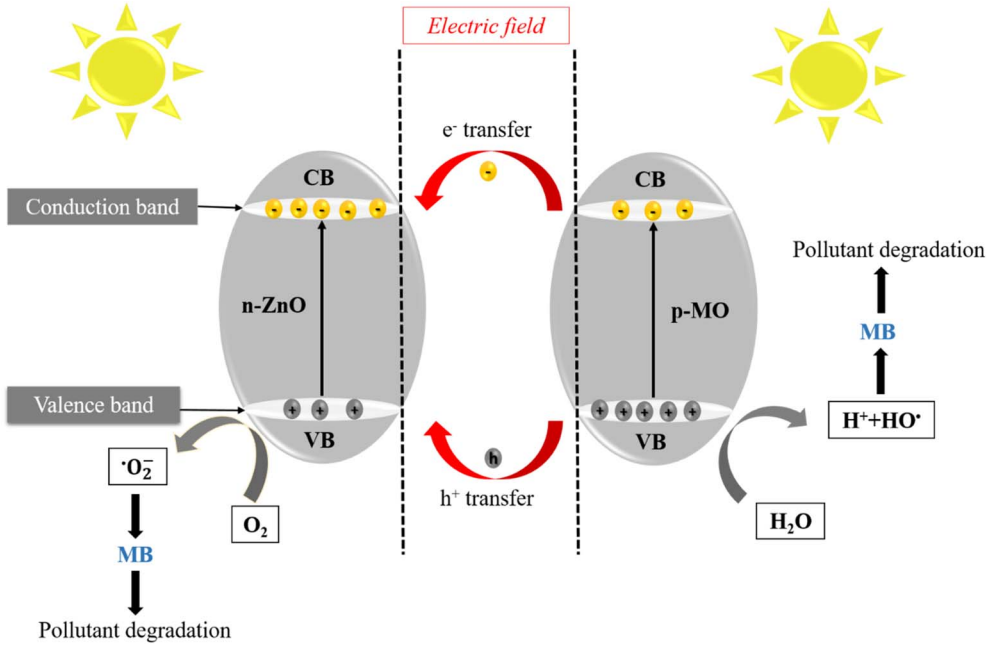

Fig. 11 The possible photocatalytic mechanism for ZnO/MO photocatalyst.

$$(e^{-})_{ZnO} + O_2 \rightarrow O_2^{\bullet -} \quad \text{(I)}$$

$$O_2^{\bullet -} + H^+ \rightarrow HO_2^{\bullet} \quad \text{(II)}$$

$$2HO_2^{\bullet} \rightarrow H_2O_2 + O_2 \quad \text{(III)}$$

$$H_2O_2 + O_2^{\bullet -} \rightarrow OH^{\bullet} + O_2 + OH^- \quad \text{(IV)}$$

➢ Pollutant degradation

The hydroxyl radicals ($OH^{\bullet}$) are known to be very reactive oxidative species; it can degrade pollutants to CO_2 and H_2O:

$$OH^{\bullet} + MB \rightarrow CO_2 \text{ (carbon dioxide)} + H_2O \text{ (water)}$$

4. Conclusion

In summary, the ZnO (n)/MO (p) {Mn_3O_4; Fe_3O_4; CuO; NiO} heterojunction photocatalysts were successfully synthesized by an inexpensive and eco-friendly hydrothermal method. The structural and morphological results proved that the coupling of ZnO with MO did not provoke the ions substitution in the ZnO lattices and that the hexagonal wurtzite structure is not affected. Optical measurements revealed the presence of two gaps in the ZnO/MO composites with low values. This shows that the coupling reduces the electron–hole recombination rate, which promotes the absorption in the visible region and leads to photocatalytic performance of ZnO/MO under sunlight. The photocatalytic results indicate that the binary nanocomposite catalyst ZnO/Fe_3O_4 has a great potential for MB removal compared to other catalysts due to its nano-size and their activation in visible light. Therefore, due to its high photocatalytic performance, ZnO/Fe_3O_4 can be exploited as an effective material for water decontamination. We hope that our study will contribute to the development of ternary and quaternary metal oxide nanocomposites with outstanding performance and low cost to open up new opportunities for ZnO-based nanomaterials in the next generation for environmental applications.

Conflicts of interest

There are no conflicts to declare.

Acknowledgements

Authors gratefully thank the financial support of the Tunisian Ministry of higher education and scientific research, and Campus France within program (PHC Utique project No. 17G1143).

References

1 J. Ahmed, A. Thakur and A. Goyal, Chapter 1: Industrial wastewater and its toxic effects, in *Biological Treatment of Industrial Wastewater*, 2021, pp. 1–14.
2 S. Madhav, A. Ahamad, P. Singh and P. K. Mishra, A review of textile industry: Wet processing, environmental impacts, and effluent treatment methods, *Environ. Qual. Manag.*, 2018, **27**, 31–41.
3 I. A. Saleh, N. Zouari and M. A. Al-Ghouti, Removal of pesticides from water and wastewater: Chemical, physical and biological treatment approaches, *Environ. Technol. Innovation*, 2020, **19**, 101026.
4 I. Khan, K. Saeed, I. Zekker, B. Zhang, A. H. Hendi, A. Ahmad, S. Ahmad, N. Zada, H. Ahmad, L. A. Shah and T. Shah,

Review on Methylene Blue: Its Properties, Uses, Toxicity and Photodegradation, *Water*, 2022, **14**, 242.

5 H. N. Hamad and S. Idrus, Recent Developments in the Application of Bio-Waste-Derived Adsorbents for the Removal of Methylene Blue from Wastewater: A Review, *Polym*, 2022, **14**, 783.

6 P. K. Pandis, C. Kalogirou, E. Kanellou, C. Vaitsis, M. G. Savvidou, G. Sourkouni, A. A. Zorpas and C. Argirusis, Key Points of Advanced Oxidation Processes (AOPs) for Wastewater, Organic Pollutants and Pharmaceutical Waste Treatment: A Mini Review, *Chem. Engineering*, 2022, **6**, 8.

7 L. Wang, P. R. Cai and Z. Z. Liu, Role of carbon quantum dots on nickel titanate to promote water oxidation reaction under visible light illumination, *J. Colloid Interface Sci.*, 2022, **607**, 203–209.

8 S. Sakthivel, B. Neppolian, M. V. Shankar, B. Arabindoo, M. Palanichamy and V. Murugesan, Solar photocatalytic degradation of azo dye: comparison of photocatalytic efficiency of ZnO and TiO_2, *Sol. Energy Mater.*, 2003, **77**, 65–82.

9 L. Zheng, S. Han, H. Liu, P. Yu and X. Fang, Hierarchical MoS_2 nanosheet@TiO_2 nanotube array composites with enhanced photocatalytic and photocurrent performances, *Small*, 2016, **12**, 1527–1536.

10 J. Wang, R. Chen, L. Xiang and S. Komarneni, Synthesis, properties and applications of ZnO nanomaterials with oxygen vacancies: a review, *Ceram. Int.*, 2018, **44**, 7357–7377.

11 G. K. Weldegebrieal, Synthesis method, antibacterial and photocatalytic activity of ZnO nanoparticles for azo dyes in wastewater treatment: A review, *Inorg. Chem. Commun.*, 2020, **120**, 108140.

12 J. Fang, H. Fan, Y. Ma, Z. Wang and Q. Chang, Surface defects control for ZnO nanorods synthesized by quenching and their anti-recombination in photocatalysis, *Appl. Surf. Sci.*, 2015, **332**, 47–54.

13 S. G. Kumar and K. K. Rao, Comparison of modification strategies towards enhanced charge carrier separation and photocatalytic degradation activity of metal oxide semiconductors (TiO_2, WO_3 and ZnO), *Appl. Surf. Sci.*, 2017, **391**, 124–148.

14 J. Kegel, I. M. Povey and M. E. Pemble, Zinc oxide for solar water splitting: A brief review of the material's challenges and associated opportunities, *Nano Energy*, 2018, **54**, 409–428.

15 T. U. D. Thi, T. T. Nguyen, Y. D. Thi, K. H. T. Thi, B. T. Phan and K. N. Pham, Green synthesis of ZnO nanoparticles using orange fruit peel extract for antibacterial activities, *RSC Adv.*, 2020, **10**, 23899–23907.

16 F. M. Sanakousar, C. Vidyasagar, V. M. Jiménez-Pérez and K. Prakash, Recent progress on visible-light-driven metal and non-metal doped ZnO nanostructures for photocatalytic degradation of organic pollutants, *Mater. Sci. Semicond. Process.*, 2022, **140**, 106390.

17 S. G. Kumar and K. K. Rao, Comparison of modification strategies towards enhanced charge carrier separation and photocatalytic degradation activity of metal oxide semiconductors (TiO_2, WO_3 and ZnO), *Appl. Surf. Sci.*, 2017, **391**, 124–148.

18 L. Zheng, F. Teng, X. Ye, H. Zheng and X. Fang, Photo/electrochemical applications of metal sulfide/TiO_2 heterostructures, *Adv. Energy Mater.*, 2020, **10**, 1902355.

19 S. Han, Y. C. Pu, L. Zheng, J. Z. Zhang and X. Fang, Shell-thickness dependent electron transfer and relaxation in type-II core–shell CdS/TiO_2 structures with optimized photoelectrochemical performance, *J. Mater. Chem. A*, 2015, **3**, 22627–22635.

20 W. Ouyang, f. Teng, J. H. He and X. Fang, Enhancing the Photoelectric Performance of Photodetectors Based on Metal Oxide Semiconductors by Charge Carrier Engineering, *Adv. Funct. Mater.*, 2019, **29**, 1807672.

21 S. A. Kulkarni, P. S. Sawadh, P. K. Palei and K. K. Kokate, Effect of synthesis route on the structural, optical and magnetic properties of Fe_3O_4 nanoparticles, *Ceram. Int.*, 2014, **40**, 1945–1949.

22 B. J. Rani, M. Ravina, G. Ravi, S. Ravichandran, V. Ganesh and R. Yuvakkumar, Synthesis and characterization of hausmannite (Mn_3O_4) nanostructures, *Surf. Interfaces*, 2018, **11**, 28–36.

23 H. Abbas, K. Nadeem, A. Hafeez, A. Hassan, N. Saeed and H. Krenn, A comparative study of magnetic, photocatalytic and dielectric properties of NiO nanoparticles synthesized by sol-gel and composite hydroxide mediated method, *Ceram. Int.*, 2019, **45**, 17289–17297.

24 L. Gnanasekaran, R. Hemamalini, R. Saravanan, K. Ravichandran, F. Gracia, S. Agarwal and V. K. Gupta, Synthesis and characterization of metal oxides (CeO_2, CuO, NiO, Mn_3O_4, SnO_2 and ZnO) nanoparticles as photo catalysts for degradation of textile dyes, *J. Photochem. Photobiol., B*, 2017, **173**, 43–49.

25 H. Abbas, K. Nadeem, A. Hafeez, A. Hassan, N. Saeed and H. Krenn, A comparative study of magnetic, photocatalytic and dielectric properties of NiO nanoparticles synthesized by sol-gel and composite hydroxide mediated method, *Ceram. Int.*, 2019, **45**, 17289–17297.

26 A. Manikandan, J. J. Vijaya, J. A. Mary, L. J. Kennedy and A. Dinesh, Structural, optical and magnetic properties of Fe_3O_4 nanoparticles prepared by a facile microwave combustion method, *J. Ind. Eng. Chem.*, 2014, **20**, 2077–2085.

27 L. Bai, H. Huang, S. Yu, D. Zhang, H. Huang and Y. Zhang, Role of transition metal oxides in g-C_3N_4-based heterojunctions for photocatalysis and supercapacitors, *J. Energy Chem.*, 2022, **64**, 214–235.

28 J. A. Lett, S. F. Alshahateet, I. Fatimah, R. P. Sivasankaran, A. K. Sibhatu, M. V. Le and S. Sagadevan, Hydrothermal Synthesis and Photocatalytic Activity of Mn_3O_4 Nanoparticles, *Top. Catal.*, 2022, 1–13.

29 Q. Li, J. Meng, J. Huang and Z. Li, Plasmon-induced pyro-phototronic effect enhancement in self-powered UV-vis detection with a ZnO/CuO p–n junction device, *Adv. Funct. Mater.*, 2022, **32**, 2108903.

30 P. Salunkhe, P. Bhat and D. Kekuda, Performance evaluation of transparent self-powered n-ZnO/p-NiO heterojunction

ultraviolet photosensors, *Sens. Actuators, A*, 2022, **345**, 113799.

31 J. Li, F. Zhao, L. Zhang, M. Zhang, H. Jiang, S. Li and J. Li, Electrospun hollow ZnO/NiO heterostructures with enhanced photocatalytic activity, *RSC Adv.*, 2015, **5**, 67610–67616.

32 A. E. Ramírez, M. Montero-Muñoz, L. L. López, J. E. Ramos-Ibarra, J. A. Coaquira, B. Heinrichs and C. A. Páez, Significantly enhancement of sunlight photocatalytic performance of ZnO by doping with transition metal oxides, *Sci. Rep.*, 2021, **11**, 1–9.

33 E. D. Sherly, J. J. Vijaya, L. J. Kennedy, A. Meenakshisundaram and M. Lavanya, A comparative study of the effects of CuO, NiO, ZrO_2 and CeO_2 coupling on the photocatalytic activity and characteristics of ZnO, *Korean J. Chem. Eng.*, 2016, **33**, 1431–1440.

34 M. Kashif, M. Fiaz and M. Athar, One-step hydrothermal synthesis of ZnO nanorods as efficient oxygen evolution reaction catalyst, *Inorg. Nano-Met. Chem.*, 2022, **52**, 101–107.

35 S. Valencia, J. M. Marín and G. Restrepo, Study of the bandgap of synthesized titanium dioxide nanoparticles using the sol-gel method and a hydrothermal treatment, *Open Mater. Sci. J.*, 2010, **4**, 9–14.

36 J. Nyika, E. Onyari, M. Dinka and S. Mishra, Analysis of particle size distribution of landfill contaminated soils and their mineralogical composition, *Part. Sci. Technol.*, 2020, **38**, 843–853.

37 C. Zhou, L. Xu, J. Song, R. Xing, S. Xu, D. Liu and H. Song, Ultrasensitive non-enzymatic glucose sensor based on three-dimensional network of ZnO-CuO hierarchical nanocomposites by electrospinning, *Sci. Rep.*, 2014, **4**, 1–9.

38 S. H. Choi and Y. C. Kang, Using Simple Spray Pyrolysis to Prepare Yolk–Shell-Structured ZnO–Mn3O4 Systems with the Optimum Composition for Superior Electrochemical Properties, *Chem.–Eur. J.*, 2014, **20**, 3014–3018.

39 M. Farrokhi, S. C. Hosseini, J. K. Yang and M. Shirzad-Siboni, Application of ZnO–Fe_3O_4 Nanocomposite on the Removal of Azo Dye from Aqueous Solutions: Kinetics and Equilibrium Studies, *Water, Air, Soil Pollut.*, 2014, **225**, 2113.

40 L. Qiao, X. Wang, X. Sun, X. Li, Y. Zheng and D. He, Single electrospun porous NiO–ZnO hybrid nanofibers as anode materials for advanced lithium-ion batteries, *Nanoscale*, 2013, **5**, 30423037.

41 A. Badawi, M. G. Althobaiti, E. E. Ali, S. S. Alharthi and A. N. Alharbi, A comparative study of the structural and optical properties of transition metals (M = Fe, Co, Mn, Ni) doped ZnO films deposited by spray-pyrolysis technique for optoelectronic applications, *Opt. Mater.*, 2022, **124**, 112055.

42 M. M. B. Mohagheghi, N. Shahtahmasebi and M. R. Alinejad, The Scherrer formula for X-ray particle size determination, *Phys. Rev.*, 1939, **56**, 978–982.

43 Y. Gao, L. Bai, X. Zhang and F. Yang, Non-Parallel photo-assisted electrocatalysis mechanism of SnS_2/NiO heterojunction for efficient electrocatalytic oxygen evolution Reaction, *ChemElectroChem*, 2021, **8**, 2087–2093.

44 P. Zhu, X. Yin and X. Gao, Enhanced photocatalytic NO removal and toxic NO_2 production inhibition over ZIF-8-derived ZnO nanoparticles with controllable amount of oxygen vacancies, *Chin. J. Catal.*, 2021, **42**, 175–183.

45 N. Khlifi, S. Mnif, F. B. Nasr, N. Fourati, C. Zerrouki, M. M. Chehimi, H. Guermazi, S. Aifaband and S. Guermazi, Non-doped and transition metal-doped CuO nano-powders: structure-physical properties and anti-adhesion activity relationship, *RSC Adv.*, 2022, **12**, 23527–23543.

46 M. Sajjad, I. Ullah, M. I. Khan, J. Khan, M. Y. Khan and M. T. Qureshi, Structural and optical properties of pure and copper doped zinc oxide nanoparticles, *Results Phys.*, 2018, **9**, 1301–1309.

47 M. Andrade-Guel, C. Cabello-Alvarado, P. Bartolo-Pérez, D. I. Medellin-Banda, C. A. Ávila-Orta, B. Cruz-Ortiz and G. C. Pliego, Surface modification of TiO_2/ZnO nanoparticles by organic acids with enhanced methylene blue and rhodamine B dye adsorption properties, *RSC Adv.*, 2022, **12**, 28494–28504.

48 A. S. Alshammari, L. Chi, X. Chen, A. Bagabas, D. Kramer, A. Alromaeh and Z. Jiang, Visible-light photocatalysis on C-doped ZnO derived from polymer-assisted pyrolysis, *RSC Adv.*, 2015, **5**, 27690–27698.

49 M. Saleem and D. Varshney, Structural, thermal, and transport properties of $La_{0.67}$ $Sr_{0.33}$ MnO_3 nanoparticles synthesized *via* the sol–gel auto-combustion technique, *RSC Adv.*, 2018, **8**, 1600–1609.

50 Y. Mao, B. Qiu, P. Li, X. Liu and S. M. Chen, Ultrasonic-assisted synthesis $Zn_{0.78}Cd_{0.22}S$/Bi_2MoO_6 heterojunction to improve photocatalytic performance for hexavalent chromium removal and hydrogen peroxide production, *Colloids Surf., A*, 2022, 129363.

51 A. Naseri, M. Goodarzi and D. Ghanbari, Green synthesis and characterization of magnetic and effective photocatalyst $NiFe_2O_4$–NiO nanocomposites, *J. Mater. Sci.: Mater. Electron.*, 2017, **28**, 17635–17646.

52 R. Carrera, A. L. Vázquez, S. Castillo and E. M. Arce Estrada, Photocatalytic degradation of acetaldehyde by sol-gel TiO_2 nanoparticles: Effect of the physicochemical properties on the photocatalytic activity, *Mater. Sci. Forum*, 2011, **691**, 92–98.

53 H. Yu, J. Huang, L. Jiang, X. Yuan, K. Yi, W. Zhang and H. Chen, Steering photo-excitons towards active sites: Intensified substrates affinity and spatial charge separation for photocatalytic molecular oxygen activation and pollutant removal, *Chem. Eng. J.*, 2021, **408**, 127334.

54 S. Kanan, M. A. Moyet, R. B. Arthur and H. H. Patterson, Recent advances on TiO_2-based photocatalysts toward the degradation of pesticides and major organic pollutants from water bodies, *Catal. Rev.: Sci. Eng.*, 2020, **62**, 1–65.

55 M. Pirhashemi, A. Habibi-Yangjeh and S. R. Pouran, Review on the criteria anticipated for the fabrication of highly efficient ZnO-based visible-light-driven photocatalysts, *J. Ind. Eng. Chem.*, 2018, **62**, 1–25.

56 J. C. Ragain Jr and W. M. Johnston, Accuracy of Kubelka-Munk reflectance theory applied to human dentin and enamel, *J. Dent. Res.*, 2001, **80**, 449–452.

57 J. Tauc, R. Grigorovici and A. Vancu, Optical properties and electronic structure of amorphous germanium, *Phys. Status Solidi*, 1966, **15**, 627–637.

58 S. Yasmeen, F. Iqbal, T. Munawar, M. A. Nawaz, M. Asghar and A. Hussain, Synthesis, structural and optical analysis of surfactant assisted ZnO–NiO nanocomposites prepared by homogeneous precipitation method, *Ceram. Int.*, 2019, **45**, 17859–17873.

59 S. Chabri, A. Dhara, B. Show, D. Adak, A. Sinha and N. Mukherje, Mesoporous CuO-ZnO p–n heterojunction with high specific surface area for enhanced photocatalysis and electrochemical sensing, *Catal. Sci. Technol.*, 2018, **6**, 3238–3252.

60 M. T. Qamar, M. Aslam, Z. A. Rehan, M. T. Soomro, J. M. Basahi, I. M. Ismail and A. Hameed, The influence of p-type Mn_3O_4 nanostructures on the photocatalytic activity of ZnO for the removal of bromo and chlorophenol in natural sunlight exposure, *Appl. Catal., B*, 2017, **201**, 105–118.

61 A. Anu and M. Abdul Khadar, CuO–ZnO nanocomposite films with efficient interfacial charge transfer characteristics for optoelectronic applications, *SN Appl. Sci.*, 2019, **1**, 1057.

62 R. K. Sharma, D. Kumar and R. Ghose, Synthesis of nanocrystalline ZnO–NiO mixed metal oxide powder by homogeneous precipitation method, *Ceram. Int.*, 2016, **42**, 4090–4098.

63 S. G. Kumar and K. K. Rao, Comparison of modification strategies towards enhanced charge carrier separation and photocatalytic degradation activity of metal oxide semiconductors (TiO_2, WO_3 and ZnO), *Appl. Surf. Sci.*, 2017, **391**, 124–148.

64 J. Liqiang, Q. Yichun, W. Baiqi, L. Shudan, J. Baojiang, Y. Libin and S. Jiazhong, Review of photoluminescence performance of nano-sized semiconductor materials and its relationships with photocatalytic activity, *Sol. Energy Mater. Sol. Cells*, 2016, **90**, 1773–1787.

65 R. K. Sharma, D. Kumar and R. Ghose, Synthesis of nanocrystalline ZnO–NiO mixed metal oxide powder by homogeneous precipitation method, *Ceram. Int.*, 2016, **42**, 4090–4098.

66 T. Tangcharoen, W. Klysubun and C. Kongmark, Synthesis of nanocrystalline NiO/ZnO heterostructured composite powders by sol-gel auto combustion method and their characterizations, *J. Mol. Struct.*, 2018, **1156**, 524–533.

67 T. Munawar, F. Iqbal, S. Yasmeen, K. Mahmood and A. Hussain, Multi metal oxide NiO-CdO-ZnO nanocomposite–synthesis, structural, optical, electrical properties and enhanced sunlight driven photocatalytic activity, *Ceram. Int.*, 2019, **46**, 2421–2437.

68 J. I. Pankove, I. Jacques and A. David, Optical Processes in Semiconductors, *J. Electrochem. Soc.*, 1972, **119**, 156.

69 S. A. Empedocles, R. Neuhauser, K. Shimizu and M. G. Bawendi, Photoluminescence from single semiconductor nanostructures, *Adv. Mater.*, 1999, **11**, 1243–1256.

70 Y. C. Zhang, Z. Li, L. Zhang, L. Pan, X. Zhang, L. Wang, A. Fazal and J. J. Zou, Role of oxygen vacancies in photocatalytic water oxidation on ceria oxide: Experiment and DFT studies, *Appl. Catal., B*, 2018, **224**, 101–108.

71 Y. Gao, L. Bai, X. Zhang and F. Yang, Non-Parallel photo-assisted electrocatalysis mechanism of SnS_2/NiO heterojunction for efficient electrocatalytic oxygen evolution Reaction, *ChemElectroChem*, 2021, **8**, 2087–2093.

72 P. Zhu, X. Yin and X. Gao, Enhanced photocatalytic NO removal and toxic NO_2 production inhibition over ZIF-8-derived ZnO nanoparticles with controllable amount of oxygen vacancies, *Chin. J. Catal.*, 2021, **42**, 175–183.

73 V. K. Gupta, R. Saravanan, S. Agarwal, F. Gracia, M. M. Khan, J. Qin and R. V. Mangalaraja, Degradation of azo dyes under different wavelengths of UV light with chitosan-SnO2 nanocomposites, *J. Mol. Liq.*, 2017, **232**, 423–430.

74 R. Saravanan, E. Sacari, F. Gracia, M. M. Khan, E. Mosquera and V. K. Gupta, Conducting PANI stimulated ZnO system for visible light photocatalytic degradation of coloured dyes, *J. Mol. Liq.*, 2016, **221**, 1029–1033.

75 R. Saravanan, V. K. Gupta, V. Narayanan and A. Stephen, Comparative study on photocatalytic activity of ZnO prepared by different methods, *J. Mol. Liq.*, 2013, **181**, 133–141.

76 L. Gnanasekaran, R. Hemamalini and K. Ravichandran, Synthesis and characterization of TiO_2 quantum dots for photocatalytic application, *J. Saudi Chem. Soc.*, 2015, **19**, 589–594.

77 H. Wang, C. Xie, W. Zhang, S. Cai, Z. Yang and Y. Gui, Comparison of dye degradation efficiency using ZnO powders with various size scales, *J. Hazard. Mater.*, 2007, **141**, 645–652.

78 A. Khatri and P. S. Rana, Visible Light Assisted Enhanced Photocatalytic Performance of ZnO/NiO Nanocomposites Prepared by Chemical Co-Precipitation Method, *J. Nanosci. Nanotechnol.*, 2019, **19**, 5233–5240.

79 T. Welderfael, M. Pattabi and R. M. Pattabi, Photocatalytic activity of Ag-N co-doped ZnO nanorods under visible and solar light irradiations for MB degradation, *J. Water Process. Eng.*, 2019, **14**, 117–123.

80 A. Mahana, O. I. Guliy, S. C. Momin, R. Lalmuanzeli and S. K. Mehta, Sunlight-driven photocatalytic degradation of methylene blue using ZnO nanowires prepared through ultrasonication-assisted biological process using aqueous extract of *Anabaena doliolum*, *Opt. Mater.*, 2020, **108**, 110205.

81 R. Saravanan, S. Karthikeyan, V. K. Gupta, G. Sekaran, V. Narayanan and A. Stephen, Enhanced photocatalytic activity of ZnO/CuO nanocomposite for the degradation of textile dye on visible light illumination, *Mater. Sci. Eng., C*, 2013, **33**, 91–98.

82 M. Shekofteh-Gohari and A. Habibi-Yangjeh, Novel magnetically separable ZnO/AgBr/Fe_3O_4/Ag_3VO_4 nanocomposites with tandem n–n heterojunctions as highly efficient visible-light-driven photocatalysts, *RSC Adv.*, 2016, **6**, 2402–2413.

83 J. P. Shubha, S. F. Adil, M. Khan, M. R. Hatshan and A. Khan, Facile Fabrication of a ZnO/Eu_2O_3/NiO-Based Ternary Heterostructure Nanophotocatalyst and Its Application for the Degradation of Methylene Blue, *ACS Omega*, 2021, **6**, 3866–3874.

84 H. Rahaman and S. K. Ghosh, Soft-templated synthesis of Mn_3O_4 microdandelions for the degradation of alizarin red under visible light irradiation, *RSC Adv.*, 2016, **6**, 4531–4539.

85 H. M. Chenari, R. Zamiri, D. M. Tobaldi, M. Shabani, A. Rebelo, J. S. Kumar, S. A. Salehizadeh, M. P. F. Graça, M. J. Soares, J. A. Labrincha and J. M. F. Ferreira, Nanocrystalline ZnO–SnO_2 mixed metal oxide powder: microstructural study, optical properties, and photocatalytic activity, *J. Sol-Gel Sci. Technol.*, 2017, **84**, 274–282.

86 J. Aliaga, N. Cifuentes, G. González, C. Sotomayor-Torres and E. Benavente, Enhancement photocatalytic activity of the heterojunction of two-dimensional hybrid semiconductors ZnO/V_2O_5, *Catalysts*, 2018, **8**, 374.

87 C. B. Ong, L. Y. Ng and A. W. Mohammad, A review of ZnO nanoparticles as solar photocatalysts: Synthesis, mechanisms and applications, *Renewable Sustainable Energy Rev.*, 2018, **81**, 536–551.

88 A. Das, P. Mathan Kumar, M. Bhagavathiachari and R. G. Nair, Hierarchical ZnO-TiO_2 nanoheterojunction: A strategy driven approach to boost the photocatalytic performance through the synergy of improved surface area and interfacial charge transport, *Appl. Surf. Sci.*, 2020, **534**, 147321.

89 C. Luo, D. Li, W. Wu, Y. Zhang and C. Pan, Preparation of porous micro–nano-structure NiO/ZnO heterojunction and its photocatalytic property, *RSC Adv.*, 2014, **4**, 3090–3095.

90 P. Dhiman, G. Rana, A. Kumar, G. Sharma, D. V. N. Vo and M. Naushad, ZnO-based heterostructures as photocatalysts for hydrogen generation and depollution: a review, *Environ. Chem. Lett.*, 2022, 1–35.

91 K. Qi, B. Cheng, J. Yu and W. Ho, Review on the improvement of the photocatalytic and antibacterial activities of ZnO, *J. Alloys Compd.*, 2017, **727**, 792–820.